POTSDAM-INSTITUT FÜR KLIMAFOLGENFORSCHUNG

Editor summary:

Complex interactions between drivers have hampered efforts to understand observed changes in fire behaviour worldwide. Here, fire model ensembles and impact attribution show that climate change increasingly explain changes in global burned area

Peer review information:

Nature Climate Change thanks Nerilie Abram, Yannick le Page and the other, anonymous, reviewer(s) for their contribution to the peer review of this work.

Inventory of Supporting Information

Manuscript #: NCLIM-23071495C-Z

Corresponding author name(s): Seppe Lampe

1. Extended Data

Figure or Table #	Figure/Table title	Filename	Figure/Table Legend
Please group Extended Data items by type, in sequential order. Total	One sentence only		If you are citing a reference for the first time in these legends, please include all new references in the main text Methods References section, and carry on the numbering from the main References section of the paper. If your paper

number of items (Figs. + Tables) must not exceed 10.		Whole original file name including extension. i.e.: Smith_ED_Fig1.jpg	does not have a Methods section, include all new references at the end of the main Reference list.
Extended Data Fig. 1	Model validation for 4 selected regions	Extended_Data_Figure_1.jpg	Model validation for 4 selected regions. Distribution of models and observations for probability distribution (top row), quantile-quantile plots (middle row) and power spectra (bottom row). All show relative anomaly compared to observations. In the QQ plots, models are plotted in colours against GFED5 (dotted lines) and Fire CCI5.1 (solid lines).
Extended Data Fig. 2	Description of the general workflow	Extended_Data_Figure_2.jpg	Description of the general workflow.
Extended Data Fig. 3	Description of the weighting	Extended_Data_Figure_3.jpg	Description of the weighting. First, the burned area (BA) observations and simulations are transformed to relative anomalies. Then, we calculate the climatological RMSE and total NME of between the observational RA (monthly) and the factual simulated RA (monthly). From the RMSE, we generate random noise and add that to the simulated values. We repeat this process 1000 times, the bottom right plot is a visualization of the aggregation of these 1000 series (using yearly data instead of monthly for simplification), showing the median value for each model for each timestep along with the P2.5-P97.5. We then

			combine these 1000 series with the NME and the kneedle algorithm; to find the optimal σ_D and the according weights. This results in 1000 sets of weights (box shows the inter-quantile range (IQR) centred around the median, while the whiskers extend from the box by 1.5 times the IQR and the dots represent outliers), which are used in our analysis.
Extended Data Table. 1	Fire model overview	Extended_Data_Table_1.tiff	Fire model overview.
Extended Data Table. 2	Global benchmarking for the ranked and annual NME scores used in the model weighing.	Extended_Data_Table_2.tiff	Global benchmarking for the ranked and annual NME scores used in the model weighing. Global NME scores are heavily skewed towards models that represent the African savannahs well. The lower the NME, the better a model performs.

19

20 # 1. Supplementary Information:

21 ## A. PDF Files

22

23

Item	Present?	Filename	A brief, numerical description of file contents.

		Whole original file name including extension. i.e.: Smith_SI.pdf. The extension must be .pdf	i.e.: *Supplementary Figures 1-4, Supplementary Discussion, and Supplementary Tables 1-4.*
Supplementary Information	Yes	Burton_Lampe_etal_Supplement_Revision_4.pdf	Supplementary Text 1-5, Supplementary Figures 1-9 and Supplementary Tables 1-6.

24

Global burned area increasingly explained by climate change

Author list: Chantelle Burton[1*] and Seppe Lampe[2*], Douglas I. Kelley[3], Wim Thiery[2], Stijn Hantson[4], Nikos Christidis[1], Lukas Gudmundsson[5], Matthew Forrest[6], Eleanor Burke[1], Jinfeng Chang[7], Huilin Huang[8], Akihiko Ito[9,10], Sian Kou-Giesbrecht[11], Gitta Lasslop[6], Wei Li[12], Lars Nieradzik[13], Fang Li[14], Yang Chen[15], James Randerson[15], Christopher P.O. Reyer[16] & Matthias Mengel[16]

Affiliations:

[1] Met Office Hadley Centre, Fitzroy Road, Exeter, EX1 3PB, UK
[2] Vrije Universiteit Brussel, Department of Water and Climate, Brussels, Belgium. Corresponding author: seppe.lampe@vub.be
[3] UK Centre for Ecology and Hydrology, Wallingford, OX10 8BB, UK
[4] Faculty of Natural Sciences, Universidad del Rosario, Bogotá, Colombia
[5] Institute for Atmospheric and Climate Science, Department of Environmental Systems Science, ETH, Zurich, Zurich, Switzerland
[6] Senckenberg Biodiversity and Climate Research Centre, 60325 Frankfurt am Main, Germany
[7] College of Environmental and Resource Sciences, Zhejiang University, Hangzhou, China
[8] Pacific Northwest National Laboratory, Richland, WA, 99354, USA
[9] National Institute for Environmental Studies (NIES), 16-2 Onogawa, Tsukuba, Ibaraki, 305-8506, Japan
[10] The University of Tokyo, 1-1-1 Yayoi, Bunkyo-ku, Tokyo 113-8657, Japan
[11] Dalhousie University, Department of Earth and Environmental Sciences, Halifax, Canada
[12] Department of Earth System Science, Ministry of Education Key Laboratory for Earth System Modeling, Institute for Global Change Studies, Tsinghua University, Beijing, China
[13] Department of Physical Geography and Ecosystem Science, Lund University, Sweden
[14] International Center for Climate and Environment Sciences, Institute of Atmospheric Physics, Chinese Academy of Sciences, Beijing 100029, China
[15] Department of Earth System Science, University of California, Irvine, CA 92697, USA
[16] Potsdam Institute for Climate Impact Research, Member of the Leibniz Association, Potsdam, Germany
* equally contributed to this work

Abstract

Fire behaviour is changing in many regions worldwide. However, non-linear interactions between fire weather, fuel, land use, management, and ignitions have impeded formal attribution of global burned area changes. Here we demonstrate that climate change increasingly explains regional burned area patterns, using an ensemble of global fire models. The simulations show climate change increased global burned area by 15.8% [13.1-18.7] for 2003-2019, and increased the probability of experiencing months with above-average global burned area by 22% [18-26]. In contrast, other human forcings contributed to lowering burned area by 19.1% [21.9-15.8] over the same period. Moreover, the contribution of climate change to burned area increased by 0.22% [0.22-0.24] per year globally, with the largest increase in Central Australia. Our results highlight the importance of immediate, drastic and sustained greenhouse gas emission reductions along with landscape & fire management strategies to stabilise fire impacts on lives, livelihoods and ecosystems.

Main

Global mean temperature has already increased 1.2°C above pre-industrial levels[1], and concurrently, there is an ongoing change in fire regimes[2–4]. Over the last decade, larger and more frequent fires have been observed in regions including California, the Cerrado in Brazil, Canada, and Siberia[5]. Several regions where fires were previously rare are now seeing an increase in number and extent[5]. For example, the Siberian heatwave in 2020 caused extensive fires and was one of the first extreme events shown to be almost impossible without climate change[6]. In contrast, other regions experienced reduced fire activity mainly related to changes in land-use and suppression, leading to an overall decrease in global burned area[7,8].

Quantifying the effect of climate change on historical burned area is crucial to understanding how global fire regimes will change in the future. Future burned area projections remain uncertain[5,9], with high confidence of increases in fire frequency limited to a few tropical forests and forest-savannah transition zones, the Arctic and boreal regions, and the Mediterranean[2,5,10].

Yet the overall contribution of climate change to today's global fire regimes has not yet been quantified[2,10]. While the recent Assessment Report by the Intergovernmental Panel on Climate Change (IPCC AR6) concludes that anthropogenic climate change has '*likely* increased fire weather in some regions of all inhabited continents (medium confidence)'[11], other studies have shown a decline in global total burned area dominated by land use change in savanna regions[7]. Some studies have attributed recent fire changes in boreal, temperate and tropical ecosystems to climate-driven changes in fuel dryness and availability[2,10].

Attributing changes in burned area to human or natural causes is complicated because multiple contributing factors drive fires, including fire weather, fuel, land use, land management, and ignitions, which all may have anthropogenic and natural components. Climate change also affects precipitation patterns, vegetation growth and species distribution, which can reduce fire, even if fire weather increases[12]. Therefore, it is not enough to consider changes in fire weather only, and coupled fire-vegetation models are required for a complete picture of change. Previous attribution studies focusing on vegetation fires have often used fire danger indices[13–25], drought indices[24,26–28], or individual components of fire weather such as temperature and precipitation[29,30] which misses changes in ignitions and fuel. Observation-based approaches to modelling fire have proven useful for explaining how recent fuel and ignition changes influence burning[3,31,32]. However, as these approaches rely on observations of vegetation cover, they cannot model fire in a counterfactual world without climate change.

The IPCC AR6 Working Group II report proposes an 'impact attribution' framework to disentangle impact drivers[33–35]. In complex processes such as fire, direct human influences may counter the effects of a change in climate. For example, climate change may increase burned area, but socio-economic changes reduce it, resulting in little observed change. Impact attribution can quantify the effect of climate change on systems where multiple contributing factors result in little observed change in the real world[34]. Following this definition, the impacts are attributed to climate change but not to the causes of climate change (see 'Impact Attribution' in the Supplementary Information).

In this study, we individually attribute historical changes in burned area to changes in observed climate (meteorological conditions and CO_2) and direct human forcings (ignitions and land-use change) within this IPCC framework[33,36]. Two historical simulations were performed with seven dynamic fire-vegetation models[37] from the Inter-Sectoral Impact Model Intercomparison Project[38] (ISIMIP; Extended Data Table 1): one experiment using reanalysis climate and historical atmospheric CO_2 forcing ("Factual"), and another employing de-trended historical climate and atmospheric CO_2 fixed at 1901 levels ("Counterfactual"). The counterfactual baseline here cannot be observed and relies on fire model simulations with a stationary climate while other relevant impact drivers evolve according to historical conditions[34]. We weighted these fire models based on agreement between observations and the factual simulations of burnt area anomalies. By comparing both factual and counterfactual ensembles globally and across IPCC regions[39] (Figure S1 and Table S1), we can attribute changes in burned area to climate change. In our analysis, we use the relative anomaly of burned area, defined as the monthly anomaly of the Factual from the Counterfactual, divided by the Counterfactual mean monthly burned area (see 'Relative Anomaly and Probability Ratio' in Methods), and consider fires to be any vegetation fire. Our

analysis uses the recent historical period 2003-2019 as the common period between the simulations and observations (see Methods).

Climate Change increases Burned Area

We first evaluate the distribution, trends, and variance of the seven fire models (Extended Data Figure 1 and Extended Data Table 2). Similar to the assessment of the previous generation of fire models[40], we find substantial differences in regional performance. Therefore, we apply a weighting using their benchmarking scores against observations and bootstrap monthly total burned area relative anomalies to obtain a weighted ensemble for each region (see Methods; Extended Data Figures 2 & 3). As the models perform better for the median than the tails of the distribution, we focus our results on median changes (see Methods).

We find a statistically significant (Table S2) shift in the distribution to higher burned area over the present-day period (2003-2019) in the factual experiment compared to the same period in the counterfactual (Figure 1a), and no difference between the two distributions in the early industrial period (1901-1917, Fig. S2). According to the simulations, global burned area increased compared to a world without climate change. The shift in the median (vertical lines, Figure 1) indicates that 15.8% [13.1-18.7] (95% CI) more area burned globally due to climate change over the 2003-2019 period.

Over the same period, we find an increase in simulated median burned area due to climate change in most regions (Figure 1b). We highlight four regions with a statistically significant signal of change that also perform well against observations in our evaluation (see 'Burned Area Distribution' in Methods; Tables S3-S4). In these regions, the median burned area for the 2003-2019 period increases by 22.4% [17.5-27.7] in Northern Australia (NAU), 28.9% [21.8-35.5] in South-Eastern South America (SES), 17.5% [12.4-22.6] in West Siberia (WSB), and 14.9% [11.6-18.4] in Western North America (WNA) due to climate change (Table S1). The regions with the highest (absolute) burned areas - that is, Central Africa, Western Africa and North-Eastern Africa - show increases in burned area due to climate change of 20.3% [16.4-24.7], 2.7% [1.9-7.8] and 12.4% [6.3-18.8], respectively.

We also quantify the effect socio-economic factors of land use and population density have on burned area. To this end, we compare the early industrial period (1901-1917) to the present (2003-2019) in the counterfactual simulations only, where the climate data have no long-term trend. Hence, the only notable change between the two time periods is due to socio-economic dynamics (land-use change, land management, and population density, which we refer to as Direct Human Forcing (DHF)). Simulated burned area decreased by 19.1% [21.9-15.8] in the present day compared to the early industrial period due to DHF globally

(Figure 1c), and in most of the IPCC regions (Figure 1d), which suggests that DHF countered the effect of climate change on burned area.

When considering all forcings combined (early industrial counterfactual compared to present-day factual), there is a slight reduction of 5.0% [7.6-2.3] in global burned area (Figure 1e), in agreement with observations[7]. However, while the net global change is small, there are larger changes on the regional scale, and the effect of climate change dominates over DHF in many regions, including Central Australia, Southern South America, and WSB. Our results highlight the importance of understanding regional changes rather than considering only the global total, especially with highly regional-specific processes such as fire.

Climate Change increases the probability of high Burned Area

We then calculate the Probability Ratio (PR)[32–35] of higher than average burned area. The PR is between the probability of being above the counterfactual median (blue areas greater than the blue vertical line, Figure 1a) under (i) the factual forcing simulation (orange shading), and (ii) the counterfactual simulation (blue shading; see 'Relative Anomaly and Probability Ratio' in Methods). This allows us to quantify how much climate change has increased the chance of above-average burning in the models.

Globally, we find a 22% [18-26] increase in the probability of above-average burned area due to climate change over the period 2003-2019 (Table S1), with this average value representing the median monthly 2003-2019 counterfactual burned area. In the four selected regions, this probability increases by 14% [11-17] in NAU, 20% [16-24] in SES, 9% [7-12] in WSB, and 11% [9-14] in WNA.

In addition to the PR above 50%, we calculate globally the PR above each percentile of the counterfactual burned area distribution from 10-90% due to climate change, DHF, and 'all forcings' combined. The PR increases across the distribution due to climate change (Figure 2), meaning that the months with the highest simulated global burned area increase the most in frequency. For example, the increase in the probability of a burned area being above the 85th percentile is approximately 2-fold (PR = 2, or a 100% increase), implying that the amount of burned area in the two most active fire months of the year would now be expected in around four months per year due to climate change. Conversely, DHF reduces the probability of burned area by about 25%. The net effect is that DHF counteracts the climate-driven increase in burned area, resulting in an overall global reduction. This offset becomes smaller in months with the largest modelled burned area (>90th percentile), as shown by 'all forcings' (Figure 2). As shown in the evaluation, the fire models do not perform well for the high tails of the distribution in some regions (Extended Data Figure 1), so results above the 90th percentile should be considered with caution. Overall, our results suggest that high-fire months are affected the most by climate change (Figure 2).

Climate Change-induced Burned Area on the Rise

We also analyse the trend over the historical period to understand how the impact of climate change on burned area is changing over time. We find a positive trend in climate change-induced burned area ("overburning") in 35 out of the 43 IPCC regions, with 13 regions showing an increase of over 0.5% year^{-1} for the 1980-2019 period (Figs. 3 and S3; Table S1). This implies that, as climate change increased over time, so has the burned area associated with climate change in most regions. Currently, we find a global increase in overburning of 0.22% year^{-1} [0.22-0.24] with respect to the counterfactual mean. In the four selected regions, this increases by 0.58% year^{-1} [0.52-0.62] in NAU, 0.79% year^{-1} [0.68-0.88] in SES, 0.64% year^{-1} [0.60-0.69] in WSB, and 0.52% year^{-1} [0.49-0.55] in WNA. The fastest increase occurs in Central Australia (3.04% year^{-1} [2.36-3.90]). In many regions, the increase from 1901 to 2019 is not linear. There is an increase in the rate at which these changes occur, especially after the 1970s, with more recent periods undergoing faster increases in climate change-induced burned area (Table S1).

Discussion

Using a weighted multi-model ensemble of coupled fire-vegetation models, our study estimates that climate change caused an increase in global burned area over the historical period and that months with the highest burned area are more affected by climate change. Many regions show a >10% increase, including all IPCC regions in Australia and several regions in South America, Siberia and North America.

We also find the relative contribution of climate change to a region's total burning is increasing rapidly. In Western America, we show an increasing trend in the influence of climate change on burned area. This aligns with recent work[41] showing increased Californian summer fires due to anthropogenic climate change. This annual rate also increases over time, indicating that trends could accelerate in the coming decades. Therefore, while DHF may have been mitigating the effects of climate change until now, our results indicate that fire regimes may be increasingly affected as the climate continues to change.

While we here show an increase in simulated burned area due to climate change, several regions worldwide have experienced a reduction in burned area overall. Regions of observed decrease are primarily savanna, grasslands and croplands, including equatorial Asia and tropical North Africa[42]. In line with previous research[7], socio-economic factors such as land-use and population have reduced climate change's impact on burned area. This implies that present-day burned area may have been even higher without the mitigating influences of fire management and suppression, landscape fragmentation, and fuel reduction, which occurred through conversion of natural areas to urban, crop, pasture, and changing landscape management practices due to socio-economic development. However, the counteracting

effect of DHF diminishes in months with higher burned areas, where climate change has the largest influence (Figure 2).

The four regions highlighted in the results represent diverse ecosystems and fire regimes, covering savannah, taiga and extra-tropical forest. NAU savanna is adapted to frequent dry season burning, and represents approximately 5% of the global burned area (Table S1). SES covers South American countries of Argentina, Uruguay, Paraguay and the far south of Brazil, mainly comprising grassland, shrub and savannah ecosystems with most burning typically occurring in the north west of the region (Fig S1), and representing approximately 2% of the global burned area. WSB is a taiga ecosystem, with infrequent burning but occasional large fires associated with coniferous forests and peat deposits accounting for 2% of the global burned area. WNA, mainly covered by temperate coniferous forest, experienced large, intense fires in recent years which have been linked with climate change and increased fuels. This region only represents 0.2% of global burned area, meaning the small relative increase in burned area has a larger impact here than in regions of high annual burned area (such as Central Africa representing 19% of global total burned area). In these four regions, our results show 10-30% increases in burned area, which can have important implications especially for ecosystems that are not fire-adapted.

In this study, we focus on changes in median burned area, as our evaluation shows that the models underestimate the highest burned areas. The nature of extreme fires means they are stochastic events, and capturing this in models is an ongoing challenge. Extreme fires as recently seen in Australia, South America and Canada offer insights into evolving fire dynamics and how we can better represent these extreme and unusual fires in our models. Figure 2 suggests that climate change predominantly impacts larger burned areas. However, as noted above, our findings are likely conservative regarding the magnitude/frequency of these high fire months. Despite these model shortcomings, we have high confidence in our results due to their grounding in observations.

Our study emphasises the importance of addressing uncertainty in fire observations and simulations to enhance the reliability of our findings. We conducted a comprehensive uncertainty analysis that integrates evidence-based estimates derived from observations and simulations (see ‘Ensemble Weighting and Uncertainty’ in Methods), allowing us to capture the complex interplay between different sources of uncertainty. By accounting for this uncertainty and providing likely ranges of climate and direct human forcings' impact on burnt area anomalies, we can show where modelled and observational evidence significantly influence both. This gives confidence in our results, which are unattainable from traditional observational or typical previous model ensemble studies.

Further development of this work could include improved parameterisation of socio-economic factors and more ensemble members. By using coupled dynamic fire-vegetation models, we model the changes in burned area over time due to climate and fuel availability

changes. Following the IPCC impact attribution framework[35], our approach also accounts for land use and ignition changes. While conducted with state-of-the-art global fire models, our simulations remain characterised by several limitations. For example, the standard way of modelling anthropogenic ignitions based on population density makes it challenging to account for regional differences in fire management. While most of the models now capture the declining global trend in burnt area due to land-use change, in some models and some regions the decline is not as large as we see in observations (e.g. the Eurasian Steppe[42]), which likely points to a need for improved parameterisation of fire-agricultural interactions. Additionally, deforestation fires are not represented in the models, which degrades model performance when evaluating our model simulations to observations in regions like South American Monsoon and North-Eastern South America. However, many of these regions also see human-induced savanna fragmentation that other studies have shown likely leads to reductions in burnt area[3,5,7,43].

Our approach to understanding the contribution of DHF to the change in burned area could be improved using additional counterfactual experiments, where socio-economic inputs are kept constant in a transient climate. Attributing changes in burned area is the first step in understanding the contribution of climate change to changes in fire impacts. Burned area is strongly correlated with fire emissions, and so our work may inform future studies on how emissions, air quality and health have been affected by climate change. Other vital impacts related to fire size and intensity are often not represented in global fire models[37,40,44,45]. Therefore, we can not assess whether the DHF effect also reduces climate effects on size and intensity, and it is recommended that future developments focus on incorporating these aspects.

Fire has significant regional impacts on human lives and ecosystems as well as more far-reaching effects on atmospheric composition, albedo, hydrology, and carbon cycling, and those impacts can be expected to increase as the climate continues to warm[46]. As for now, our models suggest that the effect of DHFs counters the effects of climate change on burned area in many regions of the world, leading to the observed stabilisation or slight decline in burned area. However, the strength of the climate change signal is increasing rapidly, suggesting stronger fire impacts on human well-being and ecosystem dynamics in the near future. Therefore, both ambitious mitigation of climate change and adaptation to the specific impacts of increasing fire risk as part of sustainable land and fire management strategies will likely be required to manage the escalating impacts of climate change-driven fires on our natural and human systems.

Acknowledgments

CB was funded by the Met Office Climate Science for Service Partnership (CSSP) Brazil project which is supported by the Department for Science, Innovation & Technology (DSIT). CB and NC were supported by the Met Office Hadley Centre Climate Programme funded by DSIT. SL was supported by a PhD Fundamental Research Grant by Fonds Wetenschappelijk Onderzoek - Vlaanderen (11M7723N). Part of the resources and services used in this work were provided by the VSC (Flemish Supercomputer Center), funded by the Research Foundation - Flanders (FWO) and the Flemish Government. DIK was supported by the Natural Environment Research Council as part of the LTSM2 TerraFIRMA project. HH is supported by United States Department of Energy, Office of Science (Lab Directed Res & Dev (LDRD) 29IN290162:80941). The Pacific Northwest National Laboratory (PNNL) is operated for DOE by the Battelle Memorial Institute under contract DE-AC05-76RLO1830. MF used resources of the Deutsches Klimarechenzentrum (DKRZ) granted by its Scientific Steering Committee (WLA) under project ID 1202. FL is supported by the National Key R&D Program of China (2022YFE0106500). WL is supported by the National Key R&D Program of China (grant number: 2019YFA0606604). JC is supported by the National Key R&D Program of China (2022YFF0801904). WT & MM acknowledge funding from the EU Horizon 2020 research and innovation program (SPARCCLE). LN is supported by the Strategic Research Area "ModElling the Regional and Global Earth system", MERGE, funded by the Swedish government and the simulations were enabled by resources provided by LUNARC, The Centre for Scientific and Technical Computing at Lund University. MM received funding from the German Federal Ministry of Education and Research (BMBF) under the research projects QUIDIC (01LP1907A) and is based upon work from COST Action CA19139 PROCLIAS (PROcess-based models for CLimate Impact Attribution across Sectors), supported by COST (European Cooperation in Science and Technology). SH acknowledges support from the Max Planck Tandem group program and from Universidad del Rosario within the program of Fondos de arranque. AI was supported by the JSPS KAKENHI Grant (no. JP21H05318). We also thank the ISIMIP core team for making these simulations possible.

Author Contributions Statement

CB and SL contributed equally to the analysis and writing. CB, SL, DK, WT, SH, NC, LG, MF designed the analysis. EB, JC, MF, HH, AI, SKG, WL ran the model simulations and contributed data. YC and JR contributed observational data. CB, SH, FL, MF, GL, CR, co-ordinated the fire sector and simulations. All authors contributed to the final manuscript.

Competing Interests Statement

The authors declare no competing interests.

Tables

Figure Legends/Captions (for main text figures)

Figure 1 | Contribution to burned area from climate change, direct human forcings and all combined*. (a, c, e) Probability density estimates*[47–50] *of the relative anomaly in global burned area (unitless), with solid lines showing the median, for (a) the present-day period (2003-2019) under factual (orange) and counterfactual (blue) climate, (c) the counterfactual simulation in the present day (purple) and early industrial (grey; 1901-1917) period, and (e) the early industrial counterfactual period (grey) and present-day factual period (green). (b, d, f) Percentage change in burned area due to (b) climate change, (d) Direct Human Forcings and (f) all forcings combined.*

Figure 2 | Dominant driver of global burned area change varies across the distribution. *Probability Ratios (PRs) of global burned area relative anomaly percentiles from climate change (orange), direct human forcings (purple), and all forcings (green). Climate change is the difference between present-day counterfactual and the present-day factual. Direct human forcings is the difference between the early-industrial counterfactual and the present-day counterfactual. All forcings is the difference between the early-industrial counterfactual and the present-day factual, where climate, CO_2, and DHF are all transient. The error bars are calculated using the 1000 ensembles, where each ensemble is a weighted resampling (n=10000). The error bars are centred around the median value and show the P2.5-P97.5 range. Note that the bars (95% percentile interval) are non-additive because of differences in the reference ensemble.*

Figure 3 | Climate change-induced increase in burned area (overburning) on the rise*. The blue line shows the overburning, which is defined here as the relative amount of additional burned area in the factual simulations compared to the counterfactual simulations of the same period (21-year window centred on the year; Equation 3). Error band represents the P10-P90 percentile interval, the thick blue line (measure of centre) is the median.*

References

1. *Forster, P. M. et al. Indicators of Global Climate Change 2022: annual update of large-scale indicators of the state of the climate system and human influence. Earth Syst Sci Data **15**, 2295–2327 (2023).*

2. *Jones, M. W. et al. Global and Regional Trends and Drivers of Fire Under Climate Change. Reviews of Geophysics **60**, e2020RG000726 (2022).*

3. *Kelley, D. I. et al. How contemporary bioclimatic and human controls change global fire regimes. Nat Clim Chang **9**, 690–696 (2019).*

4. *Bowman, D. M. J. S. et al. Vegetation fires in the Anthropocene. Nat Rev Earth Environ **1**, 500–515 (2020).*

5. *Sullivan, A. et al. Spreading like Wildfire: The Rising Threat of Extraordinary Landscape Fires. (United Nations Environment Programme, Nairobi, Kenya, 2022).*

6. *Ciavarella, A. et al. Prolonged Siberian heat of 2020 almost impossible without human influence. Clim Change **166**, 1-18 (2021).*

7. *Andela, N. et al. A human-driven decline in global burned area. Science (1979) **356**, 1356–1362 (2017).*

8. *Doerr, S. H. & Santín, C. Global trends in wildfire and its impacts: perceptions versus realities in a changing world. Philosophical Transactions of the Royal Society B: Biological Sciences **371**, 20150345 (2016).*

9. *Kloster, S. & Lasslop, G. Historical and future fire occurrence (1850 to 2100) simulated in CMIP5 Earth System Models. Glob Planet Change **150**, 58–69 (2017).*

10. *Canadell, J. G. et al. Global carbon and other biogeochemical cycles and feedbacks. in Climate Change 2021: The Physical Science Basis. Contribution of Working Group I to the Sixth Assessment Report of the Intergovernmental Panel on Climate Change (2021).*

11. *Ranasinghe, R. et al. Climate Change Information for Regional Impact and for Risk Assessment. in Climate Change 2021: The Physical Science Basis. Contribution of Working Group I to the Sixth Assessment Report of the Intergovernmental Panel on Climate Change*

(eds. Masson-Delmotte, V. et al.) (Cambridge University Press, Cambridge, UK and New York, NY, USA, 2021). doi:10.1017/9781009157896.014.

*12. Flannigan, M. D. et al. Fuel moisture sensitivity to temperature and precipitation: climate change implications. Clim Change **134**, 59–71 (2016).*

*13. Goss, M. et al. Climate change is increasing the likelihood of extreme autumn wildfire conditions across California. Environmental Research Letters **15**, 094016 (2020).*

*14. Touma, D., Stevenson, S., Lehner, F. & Coats, S. Human-driven greenhouse gas and aerosol emissions cause distinct regional impacts on extreme fire weather. Nat Commun **12**, 212 (2021).*

*15. Abatzoglou, J. T., Williams, A. P. & Barbero, R. Global Emergence of Anthropogenic Climate Change in Fire Weather Indices. Geophys Res Lett **46**, 326–336 (2019).*

*16. Abatzoglou, J. T. & Williams, A. P. Impact of anthropogenic climate change on wildfire across western US forests. Proceedings of the National Academy of Sciences **113**, 11770–11775 (2016).*

*17. Du, J., Wang, K. & Cui, B. Attribution of the extreme drought-related risk of wildfires in spring 2019 over Southwest China. Bull Am Meteorol Soc **102**, S83–S90 (2021).*

*18. Krikken, F., Lehner, F., Haustein, K., Drobyshev, I. & van Oldenborgh, G. J. Attribution of the role of climate change in the forest fires in Sweden 2018. Natural Hazards and Earth System Sciences **21**, 2169–2179 (2021).*

*19. Kirchmeier-Young, M. C., Zwiers, F. W., Gillett, N. P. & Cannon, A. J. Attributing extreme fire risk in Western Canada to human emissions. Clim Change **144**, 365–379 (2017).*

*20. Kirchmeier-Young, M. C., Gillett, N. P., Zwiers, F. W., Cannon, A. J. & Anslow, F. S. Attribution of the Influence of Human-Induced Climate Change on an Extreme Fire Season. Earths Future **7**, 2–10 (2019).*

*21. Williams, A. P. et al. Observed Impacts of Anthropogenic Climate Change on Wildfire in California. Earths Future **7**, 892–910 (2019).*

*22. Lewis, S. C. et al. Deconstructing factors contributing to the 2018 fire weather in Queensland, Australia. Bull Am Meteorol Soc **101**, S115–S122 (2020).*

*23. Hope, P. et al. On determining the impact of increasing atmospheric CO 2 on the record fire weather in eastern Australia in February 2017. Bull Am Meteorol Soc **100**, S111–S117 (2019).*

*24. Yoon, J.-H. et al. Extreme Fire Season in California: A Glimpse Into the Future? Bull Am Meteorol Soc **96**, S5–S9 (2015).*

*25. Van Oldenborgh, G. J. et al. Attribution of the Australian bushfire risk to anthropogenic climate change. Natural Hazards and Earth System Sciences Discussions **2020**, 1–46 (2020).*

*26. Partain, J. L. et al. 4. An assessment of the role of anthropogenic climate change in the Alaska fire season of 2015. Bull Am Meteorol Soc **97**, S14–S18 (2016).*

*27. Brown, T., Leach, S., Wachter, B. & Gardunio, B. The Northern California 2018 extreme fire season. Bull Am Meteorol Soc **101**, S1–S4 (2020).*

*28. Gudmundsson, L., Rego, F. C., Rocha, M. & Seneviratne, S. I. Predicting above normal wildfire activity in southern Europe as a function of meteorological drought. Environmental Research Letters **9**, 84008 (2014).*

*29. Gillett, N. P., Weaver, A. J., Zwiers, F. W. & Flannigan, M. D. Detecting the effect of climate change on Canadian forest fires. Geophys Res Lett **31**, L18211 (2004).*

*30. Tett, S. F. B. et al. 12. Anthropogenic forcings and associated changes in fire risk in western North America and Australia during 2015/16. Bull Am Meteorol Soc **99**, S60–S64 (2018).*

*31. Kelley, D. I. et al. Technical note: Low meteorological influence found in 2019 Amazonia fires. Biogeosciences **18**, 787–804 (2021).*

*32. Moritz, M. A. et al. Climate change and disruptions to global fire activity. Ecosphere **3**, 1–22 (2012).*

*33. Mengel, M., Treu, S., Lange, S. & Frieler, K. ATTRICI v1.1 - Counterfactual climate for impact attribution. Geosci Model Dev **14**, 5269–5284 (2021).*

34. O'Neill, B. et al. Key Risks Across Sectors and Regions. in Climate Change 2022: Impacts, Adaptation and Vulnerability. Contribution of Working Group II to the Sixth

Assessment Report of the Intergovernmental Panel on Climate Change (eds. Pörtner, H. O. et al.) (Cambridge University Press, Cambridge, UK and New York, NY, USA, 2022). doi:10.1017/9781009325844.025.

35. Ara Begum, R. et al. Point of Departure and Key Concepts. in Climate Change 2022: Impacts, Adaptation and Vulnerability. Contribution of Working Group II to the Sixth Assessment Report of the Intergovernmental Panel on Climate Change (eds. Pörtner, H. O. et al.) (Cambridge University Press, Cambridge, UK and New York, NY, USA, 2022). doi:10.1017/9781009325844.003.

*36. Frieler, K. et al. Scenario set-up and forcing data for impact model evaluation and impact attribution within the third round of the Inter-Sectoral Model Intercomparison Project (ISIMIP3a). EGUsphere **2023**, 1–83 (2023).*

*37. Hantson, S. et al. The status and challenge of global fire modelling. Biogeosciences **13**, 3359–3375 (2016).*

38. Burton, C. et al. ISIMIP3a Simulation Data from the Fire Sector. Preprint at https://doi.org/10.48364/ISIMIP.446106 (2024).

*39. Iturbide, M. et al. An update of IPCC climate reference regions for subcontinental analysis of climate model data: definition and aggregated datasets. Earth Syst Sci Data **12**, 2959–2970 (2020).*

*40. Hantson, S. et al. Quantitative assessment of fire and vegetation properties in simulations with fire-enabled vegetation models from the Fire Model Intercomparison Project. Geosci Model Dev **13**, 3299–3318 (2020).*

*41. Turco, M. et al. Anthropogenic climate change impacts exacerbate summer forest fires in California. Proceedings of the National Academy of Sciences **120**, e2213815120 (2023).*

*42. Chen, Y. et al. Multi-decadal trends and variability in burned area from the fifth version of the Global Fire Emissions Database (GFED5). Earth Syst Sci Data **15**, 5227–5259 (2023).*

*43. Forkel, M. et al. Emergent relationships with respect to burned area in global satellite observations and fire-enabled vegetation models. Biogeosciences **16**, 57–76 (2019).*

*44. Rabin, S. S. et al. The Fire Modeling Intercomparison Project (FireMIP), phase 1: Experimental and analytical protocols with detailed model descriptions. Geosci Model Dev **10**, 1175–1197 (2017).*

45. Burton, C. Impacts of Fire, Climate and Land-Use Change on Terrestrial Ecosystems. (University of Exeter (United Kingdom), 2018).

*46. Bowman, D. M. J. S. et al. Fire in the Earth System. Science (1979) **324**, 481–484 (2009).*

*47. Stott, P. A., Stone, D. A. & Allen, M. R. Human contribution to the European heatwave of 2003. Nature **432**, 610–614 (2004).*

*48. Stott, P. A. Attribution of regional-scale temperature changes to anthropogenic and natural causes. Geophys Res Lett **30**, 1-4 (2003).*

*49. Stott, P. A. et al. Attribution of extreme weather and climate-related events. Wiley Interdiscip Rev Clim Change **7**, 23–41 (2016).*

*50. Allen, M. Liability for climate change. Nature **421**, 891–892 (2003).*

Methods

1. Fire Models

In this study we use simulations from six fire models taking part in the ISIMIP3a fire sector, a continuation of the Fire Model Intercomparison Project (FireMIP)[37,44], plus VISIT which contributed simulations for ISIMIP3a's biome sector. A structured overview of each model is given in Extended Data Table 1. More information on how each model works is given in 'Fire Models' in the Supplementary Information.

2. Relative Anomaly and Probability Ratio

As shown in Figure S4, the spread in the absolute burned area is large amongst the observations (GFED5 has ~1.5 to 2 times more burned area than FireCCI5.1), models (350 to 750 Mha year^{-1}), and regions (0 to 127 Mha year^{-1}). Attributing changes in absolute burned area, therefore, has considerable uncertainty. Secondly, and mainly because of the observational uncertainty, this disagreement is also represented in our model simulations with some models having much higher average burned area for some regions than others. However, for most regions some models do capture the general dynamics of different regions correctly. We overcome this problem by focusing on relative changes in burned area, and use normalised relative anomaly (RA) rather than absolute burned area for our analysis. Using normalised relative anomalies also facilitates inter-regional comparison. As we report our results as *relative* change, they are always relative to a baseline (e.g., present-day counterfactual for the climate change signal) irrespective of the temporal period used, e.g., if there is 15% more burned area in the scenario than in the considered baseline, then there is an increase of 15% burned area in the average month/year. To calculate yearly RAs, we first sum the burned areas over the entire year and then calculate the RA of this yearly total burned area.

For the Probability Density Estimates (PDEs) in Figure 1, we calculate RA compared to the counterfactual mean burned area ($\overline{BA_{CF}}$). Subtracting the mean removes systematic biases, and dividing by the mean resolves the interannual variability. By comparing both factual and counterfactual experiments to the counterfactual mean, we are looking at the fractional increase in burned area driven by climate change compared to a baseline without climate change.

$$\boldsymbol{RA_{BA}} = \frac{\boldsymbol{BA} - \overline{\boldsymbol{BA_{CF}}}}{\overline{\boldsymbol{BA_{CF}}}}$$

Equation 1

Where *BA* is the time series of the monthly (global / regional) total burned area for factual (orange in Figure 1) or counterfactual (blue in Figure 1).

For evaluation in Extended Data Figure 1, we compare RA for factual simulations and observations, with anomalies calculated from their respective means ($\overline{\mathrm{BA}_{fact}}$ & $\overline{\mathrm{BA}_{obs}}$).

$$\boldsymbol{RA_{BA}} = \frac{\boldsymbol{BA} - \overline{\boldsymbol{BA}}}{\overline{\boldsymbol{BA}}}$$

Equation 2

When constructing time series in Figure 3, we are interested in the difference in burned area between the factual and counterfactual experiments through time. Interannual burned area is variable[51,52] and the counterfactual simulations have a negative trend in most regions. Therefore, we calculate this difference over a 21-year running mean centred on year *Y*, and treat the counterfactual as our baseline burned area for normalisation. By subtracting a mean, we reduce the effect of interannual variability and by choosing for a centred 21-year window mean, as opposed to the entire time series mean, we remove most of its long-term trend:

$$\boldsymbol{RA_{BA}} = \frac{\overline{\boldsymbol{BA_{21year}}} - \overline{\boldsymbol{BA_{CF21year}}}}{\overline{\boldsymbol{BA_{CF21year}}}}$$

Equation 3

Probability Ratio (PR) is the ratio of the amount of months, over the same time period, the factual and counterfactual simulations are above the counterfactual monthly mean burned area.

$$\boldsymbol{PR} = \frac{\sum(\boldsymbol{BA_F} > \overline{\boldsymbol{BA_{CF}}})}{\sum(\boldsymbol{BA_{CF}} > \overline{\boldsymbol{BA_{CF}}})}$$

Equation 4

3. Evaluation Methods

We evaluated the factual burned area simulations compared to observations for the seven fire models to assess the ensemble's ability to represent changes in burned area in each region. We constrain the model and observation data to 2003-2019, the common period of simulations and observations.

For general evaluation, we used the Normalised Mean Error (NME) metric used in previous FireMIP benchmarking[37,44,53] for spatial comparisons to quantify model performance in simulating spatial patterns of averaged burned area (Table S5), i.e. taking the mean over the temporal domain. NME_1 calculates the area-weighted absolute mean difference between

observations and simulations, normalised by the mean variation in the observations (Equation 5). We also report NME Step 3 (NME_3) from the FireMIP benchmarking framework. FireMIP recommends using NME_1 and NME_3 as they are appropriate for comparing non-normal variables such as burned area. This approach removes mean bias and absolute variance before comparison and assesses the model's ability to simulate regions of high and low burned area, and is therefore appropriate here as we are interested in relative anomalies.

$$NME_1 = \frac{\sum A_i * |obs_i - sim_i|}{\sum A_i * \left|obs_i - \overline{obs}\right|}$$

Equation 5

We also add a 'temporal NME' metric (NME_t), where we take the sum over the spatial domain (per region) and calculate the NME on the resulting time series (Tables S3-S4). This allows us to quantify the model's performance in representing the observed regional variations over time, which we assume indicates a model's ability to represent the influence of changing climate conditions on burned area. We asses each of the IPCC regions separately to match reported results and to inform model weighing (see below).

The lower the score for NME's, the closer the match between observation and simulation. For the evaluation, we also use a randomly-resampled null model, which compares a dataset generated by sampling the observations without replacement, with the observations[54]. We use the scores in conjunction with burned area maps to give context to the performance scores (Figure S1). Following[55], we also assess each model's global and regional total burned area distribution compared to the two observational datasets using probability distribution and quantile-quantile analysis. This allows us to assess which parts of burned area temporal distribution each model can reproduce i.e., do models capture low, average, or extreme burned areas.

4. Evaluation Results

Evaluation shows that no individual model captures the observations perfectly, but that at least some models in the ensemble capture the main spatial patterns and relative temporal anomalies in most IPCC regions. Most regional trends are appropriately modelled by multiple models, regions with the poorest performance are the Arabian Peninsula (ARP), West and Central Europe (WCE), South-West South-America (SWS), SAU (South Australia), and New Zealand (NZ).

4.1. General Benchmarking

Our metric scores indicate that the models reproduce the overall pattern of burned area, and perform consistently against each other globally for all products (Table S5), except VISIT. This

584 indicates that the simulated biases in VISIT compared to biases in burned area observations
585 are greater than the observed spatial variance. Considering the spatial distribution, VISIT
586 simulates the highest burned area in Australia and minimal in Africa or South America (Fig.
587 S1). SSiB4 more accurately captures the position and magnitude of Africa's Sahelian (Sahara
588 (SAH), northern Western-Africa (WAF), Central-Africa (CAF) and North Eastern-Africa (NEAF))
589 and Miomboian (Northern West Southern-Africa (WSAF) and East Southern-Africa (EASF)) fire
590 regions (Fig. S1 NME_3 of 1.06-1.14). Meanwhile, CLASSIC reproduces the magnitude of these
591 fire regions but over too extensive an area, simulating too much burning in some parts of
592 Africa with little fire in the observations. JULES Sahelian fires are reproduced but are broader
593 than in observations and shifted slightly northward into SAH. The two LPJ-GUESS models
594 simulate too low Sahelian burning. ORCHIDEE captures the Sahel, but Miomboian burning
595 extends too far into WSAF and EASF regions. However, all models estimate the relative high
596 and low fire regions fairly well, regardless of absolute magnitude, as indicated by lower NME_3
597 scores (Tables S3-S4). JULES, CLASSIC and the two LPJ models simulate more burning in the
598 Cerrado and Caatinga (North-East South-America (NES) and South-East South-America (SES))
599 than in observations, while SSiB4, ORCHIDEE and VISIT. JULES, LPJ and (to a lesser extent)
600 CLASSIC capture fires around the Amazon arc of deforestation (South-American Monsoon
601 (SAM) and the southern part of Northern South-America (NSA)). CLASSIC has too much
602 burning in South American Atlantic Forests (coastal NES). LPJ-GUESS-SIMFIRE-BLAZE captures
603 the Northern Australian (NAU) burned area, which is underestimated but present in JULES
604 and LPJ-GUESS-SPITFIRE. SSIB4 and CLASSIC burn little in NAU and have too much burning in
605 Southeastern Australia (East Australia (EAU) and South Australia (SAU)), extending too far into
606 inland Mallee and Acacia Shrublands (towards Central Australia (CAU)). CLASSIC, LPJ-GUESS-
607 SIMFIRE-BLAZE, and SSIB4 simulate the observed burning in the Kazakh (East Europe (EEU) <
608 West Siberia (WSB) and northern West Central Asia (WCA)) and Mongolian-Manchurian
609 Steppes (North East Asia (EAS) and into Russian-Far-East (RFE)) in Central and Eastern Asia,
610 though not at the observed magnitude. All models tend to burn more than observed in North
611 America, though the exact locations are model dependent.

612 **4.2. Temporal Variability**

613 We evaluate the temporal NME to assess the capability of our models in representing the
614 observed temporal patterns in burned area. An NME of 1 indicates that our models are, on
615 average, a factor of 1 away from the observed burned area RA. Here, we find that SSiB4
616 performs best globally, and ORCHIDEE-MICT-SPITFIRE has the highest NME (Extended Data
617 Table 2). However, the global trend is dominated by the African savannas, where ORCHIDEE-
618 MICT-SPITFIRE has a poor(er) performance. The full list of regional NME scores are provided
619 in Supplementary Tables S3 and S4. We find that the models tend to have low ranked monthly
620 NMEs in the Boreal regions, indicating they capture the seasonality of fires in those regions
621 relatively well. The four selected regions of interest (NAU, SES, WSB and WNA) are all

622 modelled well (NME<1) by at least multiple models in each of those regions, this holds for the
623 majority of the 43 IPCC regions. With ARP, SAU, NZ, WCA and WCE and being the regions that
624 have the poorest general performance. However, some of these regions undergo very little
625 burning and their high NME scores are partially the result of our choice to focus on the relative
626 anomaly.

627 **4.3. Burned Area Distribution**

628 Globally, the models tend to have a narrower and higher distributions than the observations
629 (Fig. S5), especially in JULES, although the LPJ models and SSiB4 match the observations more
630 closely. There is high regional variation in the distribution of burned area (Fig. S1), and the
631 global trend is dominated by Africa's Sahelian and Miomboian high burned area fire regions.
632 Regionally, VISIT stands out of the distribution in most regions (Fig. S5). Excluding VISIT (Fig.
633 S6), there are many regions where the models simulate the observed distribution well,
634 including our four selected regions (Extended Data Figure 1, top row).

635 Figure S7 shows the quantiles of the distribution for simulated and observed burned area RA.
636 Globally, the models simulate the observed distribution well, especially for the lower and
637 middle ranges of the distribution. At the very high end of the distribution, all fire models
638 simulate too little burned area compared to observations (below the 1:1 line). Regionally, this
639 is even more evident, where the models simulate much lower burned area than observed
640 generally across most regions at the top end of the distribution. This reflects how fire models
641 are designed to capture the mean burned area globally, therefore do not capture the
642 stochastic nature of burned area and extremes outside of the normal distribution[37].

643 In our selected regions, the burned area at the lower and middle end of the distribution is
644 well simulated compared to observations (Extended Data Figure 1, middle row). In SES, all the
645 models do well across the whole distribution. In other regions, especially WSB, some models
646 underestimate the observed burned area, with VISIT tending to underestimate burned area
647 RA the most compared to observations. CLASSIC performs well in WSB, and LPJ-GUESS-
648 SIMFIRE-BLAZE performs well in WNA. ORCHIDEE-MICT-SPITFIRE performs very well in WNA
649 compared to FireCCI (solid lines) but over predicts burned area compared to GFED5.

650 We also assess the variability of the models against observations with a power spectra
651 analysis (Fig. S8). Power spectra of time-varying climatic parameters illustrate their variability
652 over a range of different timescales and have been employed in attribution studies[56] to assess
653 whether the variability simulated by climate models is consistent with the one inferred from
654 observational data. Observed variability that lies within the range of the simulated spectra
655 suggests that the models provide a realistic representation, while inconsistencies can help
656 identify models that may not be fit-for purpose. Globally, the observations are within the
657 model range, although at the upper end. Regionally, there is generally good agreement

between the models and observations. In the four selected regions, the observations mostly lie in the middle to upper end of the model spread (Extended Data Figure 1, bottom row).

5. Ensemble Weighting and Uncertainty

Previous rounds of FireMIP[37] have shown individual model performance varies regionally, due to different representations of the land surface, human effects on fire and fire properties. These models rely on simplistic parameterisations of highly complex processes, including human-fire interactions. Evaluation of the previous FireMIP simulations also showed disagreement in spatial patterns across models in response to changes in climate[57]. Therefore, based on model performance in that region, we apply a region-specific weighting for each IPCC region. This approach employs an objective, evidence-based weighting for the models to ensure we include as much information as possible from the limited number of models available, whilst also highlighting regions where we have more or less uncertainty. Accurately assessing the uncertainties in fire observations[42] and simulations[7,40] is critical to have confidence in our results. Our results are, therefore, strongly informed by observations, as the models are driven with reanalysis data, and the weights are dependent on the match with observational datasets. By integrating observations from various sources alongside simulations, we capture the breadth of uncertainties inherent in fire dynamics. Our approach considers disagreements between observational datasets, biases within individual simulations regarding burnt area anomalies, and the collective performance of the ensemble relative to historical burnt area trends (see Extended Data Figures 2 & 3).

We apply a model weighting based on the model's distance to the observed burned area temporal RA[58,59]. We apply weights according to two aspects of temporal performance, which we assess for each observation (FireCCI5.1 and GFED5): (i) Do models capture the correct overall temporal variability in burned area? (ii) Do models capture year-by-year variations in burned areas? While land use and socio-economic factors can dominate long term trends in burned area[3,7], year-by-year variations are largely driven by climate and fuel dynamics[60]. Therefore, we assume inter-annual performance indicates a model's ability to simulate climate impacts on burned area.

We perform an area-weighted sum of the pixels per IPCC region for both criteria to get the regional total time series for the observations and the factual simulations. Then, we calculate the relative anomaly of the factual and the observations, as per equation (2). For the first criteria, we perform these steps on annual total burned area NME_t against each observation in turn. For the second, we perform this on ranked monthly burned areas, and again use NME to compare against both observations. This results in four NME scores (two criteria, two observations) for each model in each IPCC region (Tables S3-S4). We then sum these four NME scores to get a measure of a combined distance score (D_i), which we apply to Equation 6.

$$W_i = e^{-\frac{D_i}{\sigma_D}}$$

Equation 6

To weight the models, we use Equation 6, originally from[58], but without the denominator of the formula which deals with model (in)dependence and is relevant for large ensembles with e.g., multiple simulations of the same model. We do this for 500 different values of σ_D between 0.001 and 10, we normalize the scores per region per σ_D (so the weights (W) sum to one). σ_D scales the combined distance score, there is no analytical way to deduce its optimal value. However, close estimates can be obtained by iteratively trying out different values (see below)[58,59]. If we would have taken the mean of out four NME scores (instead of the sum), then the resulting optimal σ_D would have been four times smaller, resulting in the same weights. A large σ_d corresponds to model democracy, whereas a small σ_d focuses all the weight on the few best model(s). Therefore, using this method, we find as low a value of σ_d as possible while best matching the observations, representing a general balance between democracy and performance[59].

To measure the uncertainty in our results, we add noise by randomly sampling our modelled relative anomaly using a normal distribution centred at zero and with an absolute mean equal to the root mean squared error (RMSE) for each of the 12 climatological months. This ensures that the mean of the noise is the same as the mean of the climatological (per month) difference between simulation and observation. We do this by taking the log-transform of the modelled and observed RA, calculating the RMSE on these log-transformed RAs and generating a dataframe with random error-weighted noise (mean=0, scale=$\sqrt{\pi/2} * RMSE$). We then add the log-transformed modelled RA to this error dataframe and undo the log-transform. The reason we apply (and undo) the log-transform is to ensure our resulting RAs remain within the [-1, +∞] interval. We find the weighted mean ±1.96 weighted standard deviation of this ensemble, and assess the overlap between the model and observations and find the optimal value of σ_D. Ideally, we find the lowest σ_d where there is a 95% overlap[58,59]. However, for some regions none of the σ_D resulted in an ensemble ± 1.96SD that contained 95% of the observations. Therefore, we used the kneedle algorithm[61] to find the optimal values of σ_D. Kneedle allows to detect points in a continuous curve (ensemble performance vs σ_D) where the curvature is high. In our case this represents points where the trade-off between low σ_D and high performance is optimal (Fig. S9). We repeat this 1000 times (each time with different random noise), this gives us the optimal regional weighting of the models (1000 times), representing the best performance against observations relative to each other, along with the observation-based spread/uncertainty around those weights.

We also add the random noise to our factual and counterfactual ensemble, and then use these optimal weights to construct factual and counterfactual burned area histograms by

bootstrapping (with replacement) the monthly regional burned area RA 2003-2019 time series, where the 10 000 bootstrapped samples are assigned according to the weight for each model. Bootstrapping the models using these weights implies that we sample the best-performing models more times than models that perform poorly. We repeat this 1000 times, and measure uncertainty in all our numbers by taking the 2.5-97.5th percentile. All our results are reported as P50 [P2.5-P97.5].

Source data

Model and model input data is available from the ISIMIP data repository (https://doi.org/10.48364/ISIMIP.446106). The observational satellite burned area products FireCCI5.1 (https://doi.org/10.5285/58f00d8814064b79a0c49662ad3af537) and GFED5 (https://doi.org/10.5281/zenodo.7668424) are openly available.

Code availability

Scripts for the pre-processing and analysis are available through this GitHub repository.

743 **Methods-only references**

744 51. van der Werf, G. R. *et al.* Interannual variability in global biomass burning emissions
745 from 1997 to 2004. *Atmos Chem Phys* **6**, 3423–3441 (2006).

746 52. Tang, R. *et al.* Interannual variability and climatic sensitivity of global wildfire activity.
747 *Advances in Climate Change Research* **12**, 686–695 (2021).

748 53. Kelley, D. I. *et al.* A comprehensive benchmarking system for evaluating global
749 vegetation models. *Biogeosciences* **10**, 3313–3340 (2013).

750 54. Burton, C. *et al.* Representation of fire, land-use change and vegetation dynamics in
751 the Joint UK Land Environment Simulator vn4.9 (JULES). *Geosci Model Dev* **12**, 179–193
752 (2019).

753 55. Christidis, N., McCarthy, M. & Stott, P. A. The increasing likelihood of temperatures
754 above 30 to 40 °C in the United Kingdom. *Nat Commun* **11**, 1–10 (2020).

755 56. Gillett, N. P., Allen, M. R. & Tett, S. F. B. Modelled and observed variability in
756 atmospheric vertical temperature structure. *Clim Dyn* **16**, 49–61 (2000).

757 57. Teckentrup, L. *et al.* Response of simulated burned area to historical changes in
758 environmental and anthropogenic factors: a comparison of seven fire models.
759 *Biogeosciences* **16**, 3883–3910 (2019).

760 58. Brunner, L., Lorenz, R., Zumwald, M. & Knutti, R. Quantifying uncertainty in European
761 climate projections using combined performance-independence weighting. *Environmental*
762 *Research Letters* **14**, 124010 (2019).

763 59. Knutti, R. *et al.* A climate model projection weighting scheme accounting for
764 performance and interdependence. *Geophys Res Lett* **44**, 1909–1918 (2017).

765 60. Abatzoglou, J. T., Williams, A. P., Boschetti, L., Zubkova, M. & Kolden, C. A. Global
766 patterns of interannual climate–fire relationships. *Glob Chang Biol* **24**, 5164–5175 (2018).

767 61. Satopaa, V., Albrecht, J., Irwin, D. & Raghavan, B. Finding a 'Kneedle' in a Haystack:
768 Detecting Knee Points in System Behavior. in *2011 31st International Conference on*
769 *Distributed Computing Systems Workshops* 166–171 (2011). doi:10.1109/ICDCSW.2011.20.

Climate Change

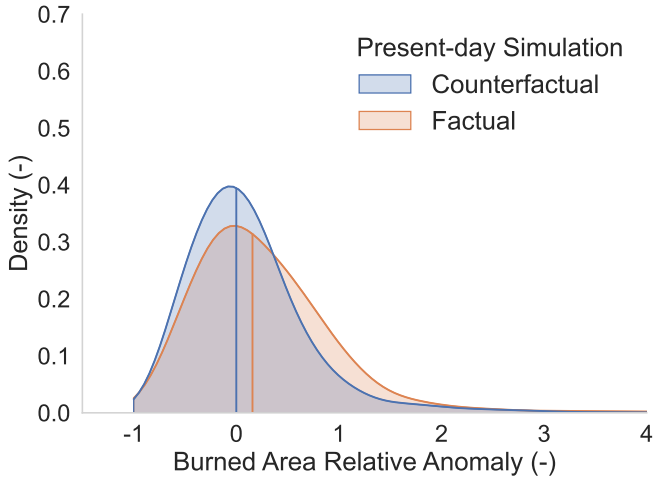

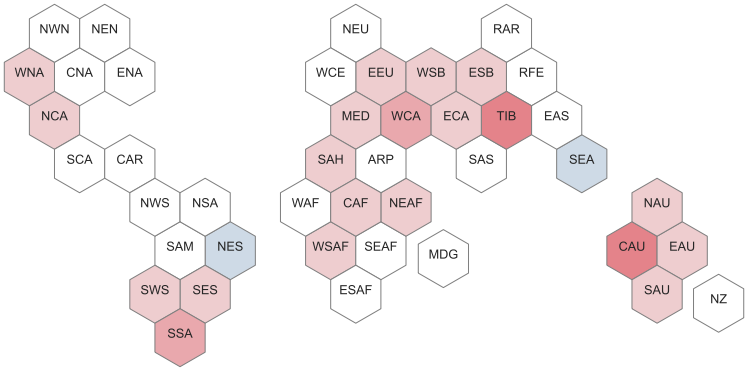

Direct Human Forcings

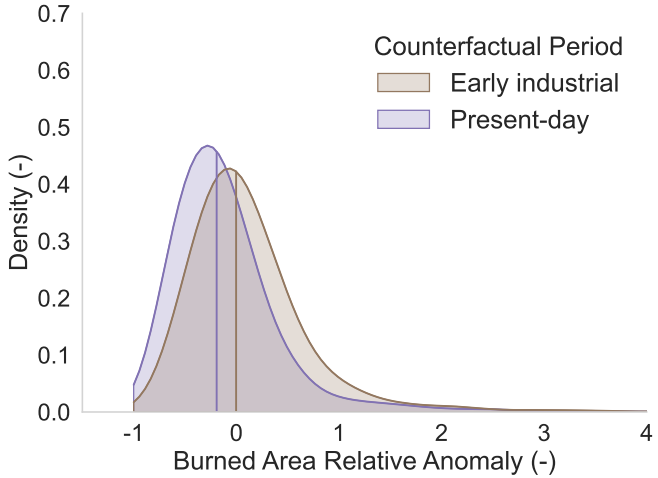

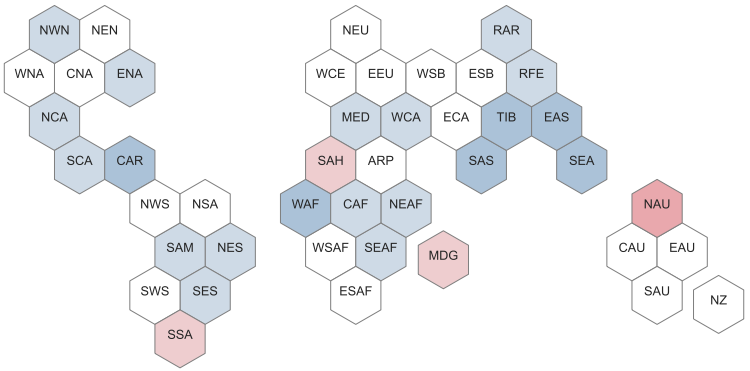

All Forcings

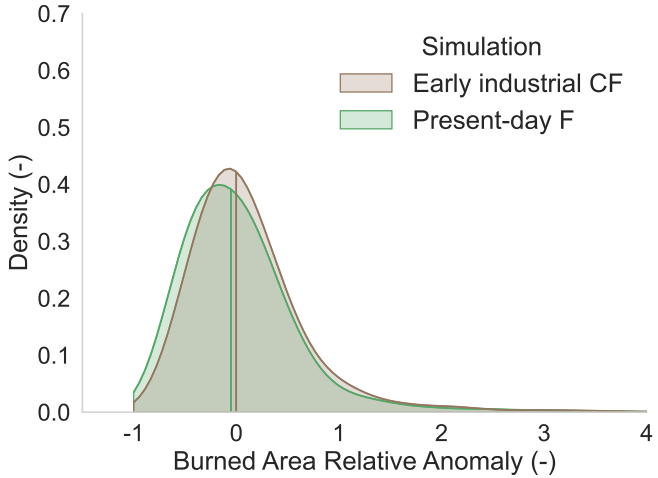

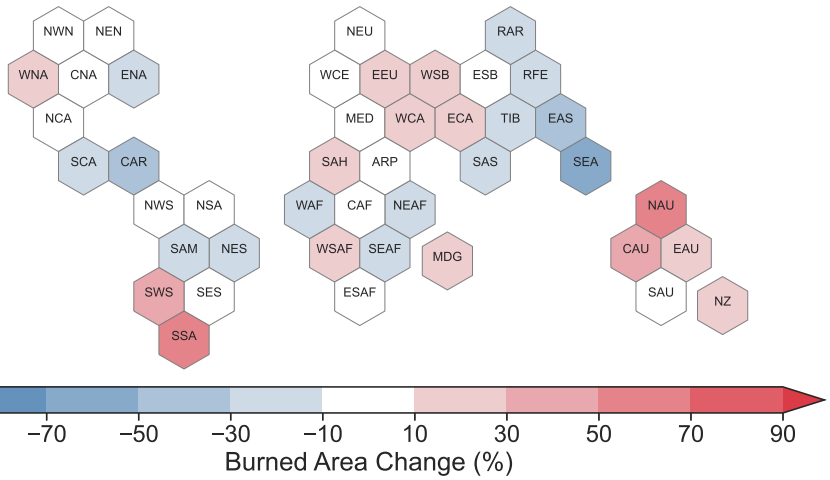

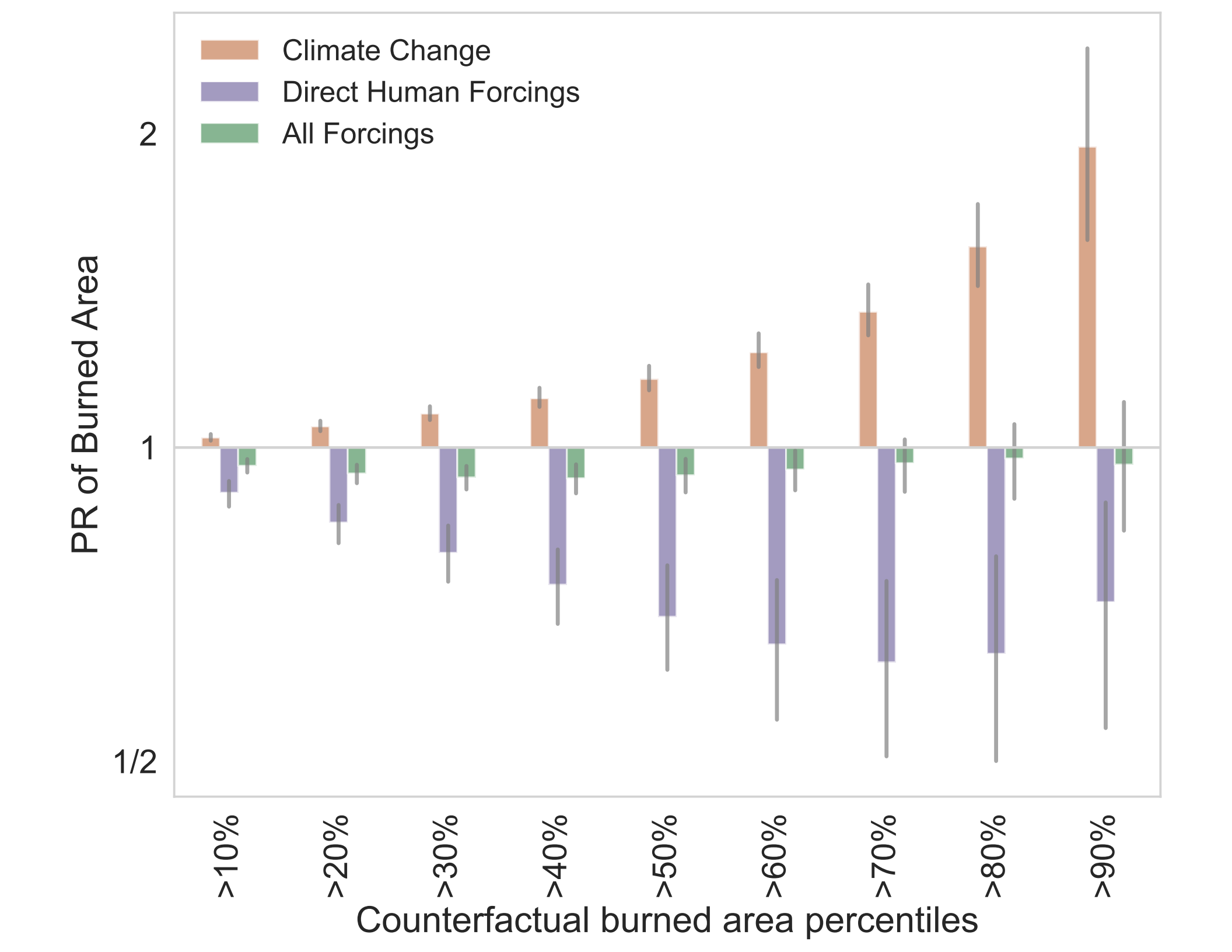
Climate Change
Direct Human Forcings
All Forcings
2
1
1/2
PR of Burned Area
>10%
>20%
>30%
>40%
>50%
>60%
>70%
>80%
>90%
Counterfactual burned area percentiles

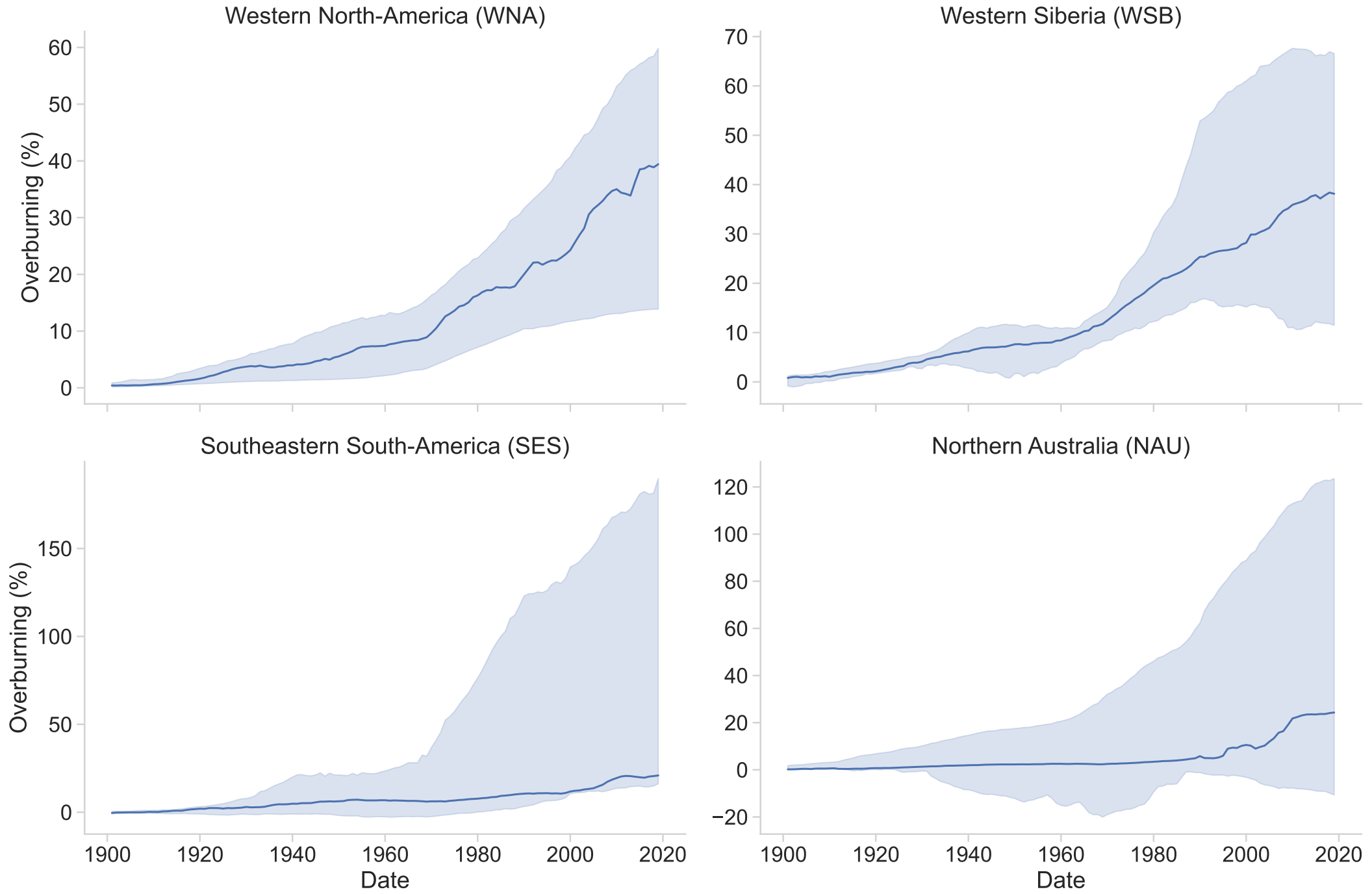
Western North-America (WNA)
Western Siberia (WSB)
Southeastern South-America (SES)
Northern Australia (NAU)
Overburning (%)
Overburning (%)
0
10
20
30
40
50
60
0
10
20
30
40
50
60
70
0
50
100
150
−20
0
20
40
60
80
100
120
1900
1920
1940
1960
1980
2000
2020
Date
Date

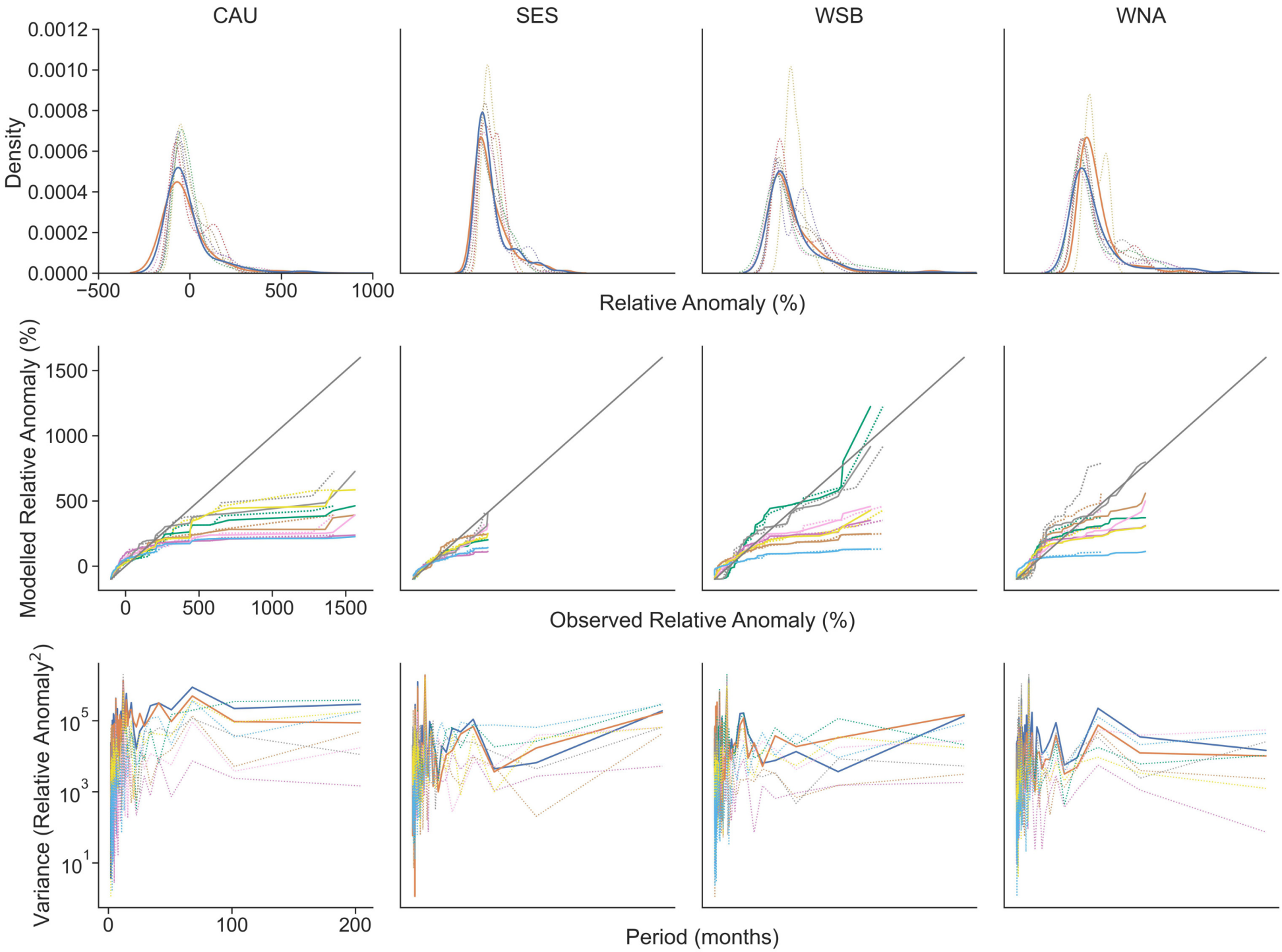
CAU
SES
WSB
WNA
Density
0.0012
0.0010
0.0008
0.0006
0.0004
0.0002
0.0000
−500
0
500
1000
Relative Anomaly (%)
Modelled Relative Anomaly (%)
1500
1000
500
0
0
500
1000
1500
Observed Relative Anomaly (%)
Variance (Relative Anomaly^2)
10^5
10^3
10^1
0
100
200
Period (months)
FireCCI5.1
GFED5
CLASSIC
JULES
LPJ-GUESS-SIMFIRE-BLAZE
LPJ-GUESS-SPITFIRE
ORCHIDEE-MICT-SPITFIRE
SSiB4
VISIT

Factual

Counterfactual

Reanalysis

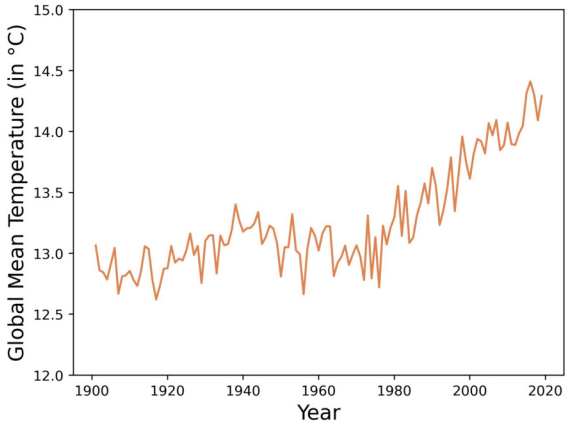

ATTRICI

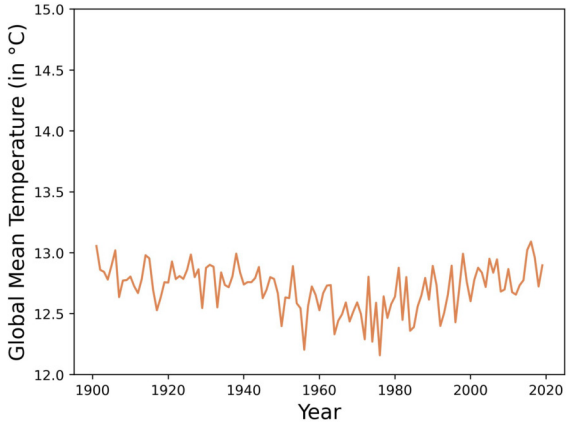

Fire Models

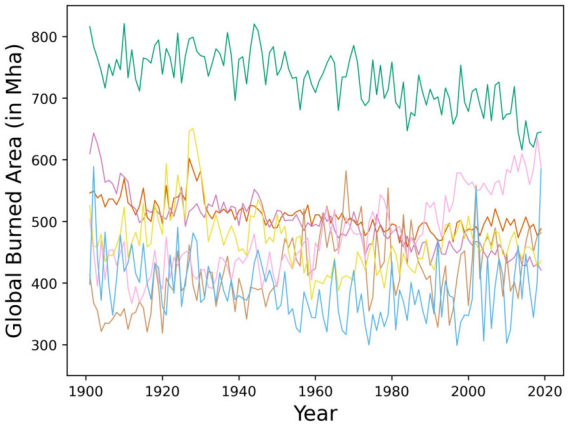

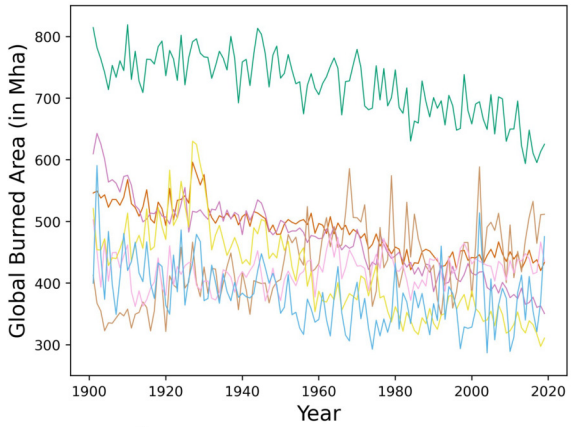

Processing

Weighting

Analysis

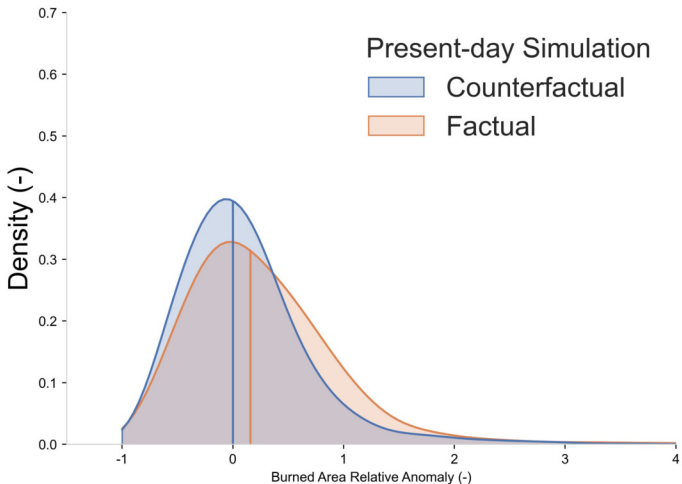

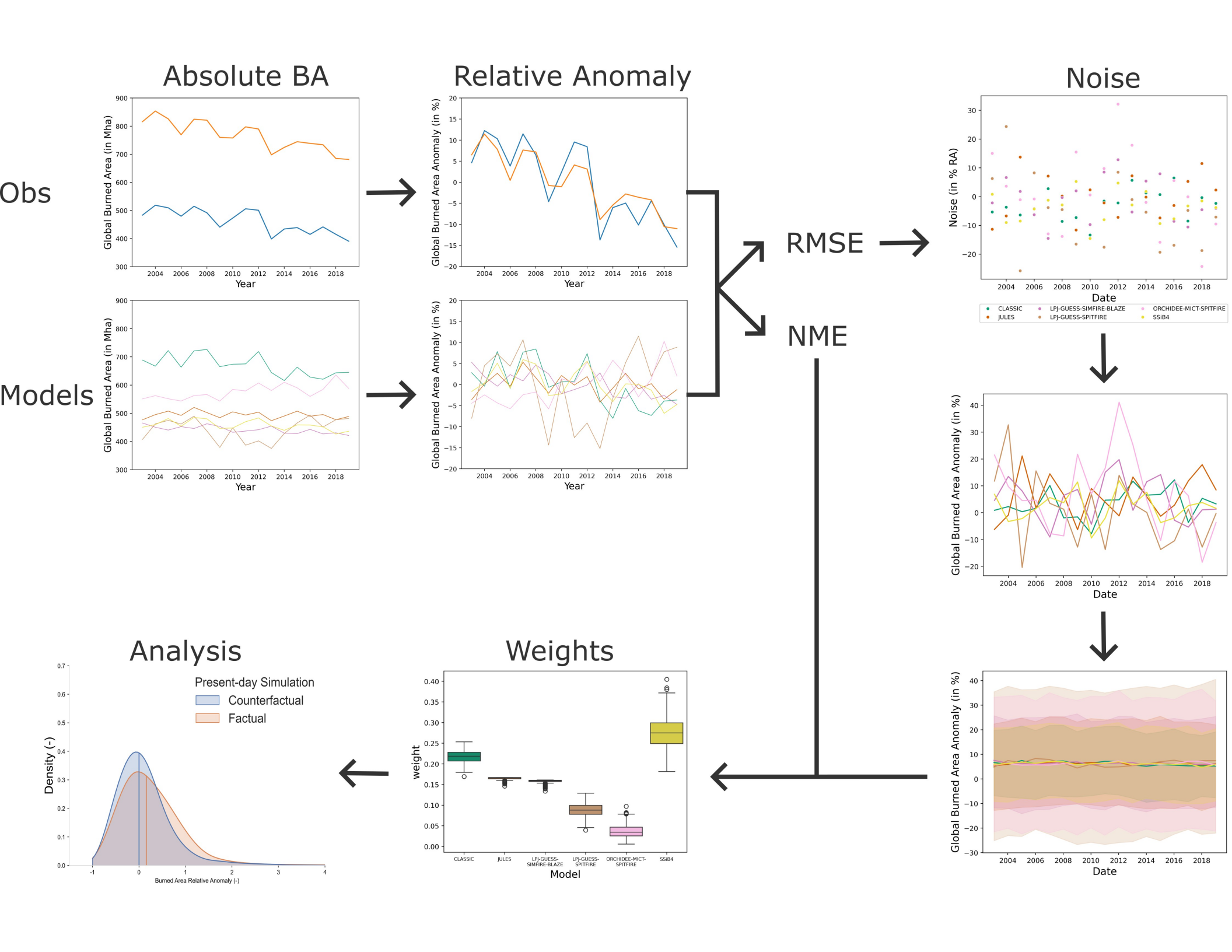
Absolute BA
Relative Anomaly
Noise
Obs
Models
RMSE
NME
Global Burned Area (in Mha)
Global Burned Area Anomaly (in %)
Noise (in % RA)
Year
Date
CLASSIC
JULES
LPJ-GUESS-SIMFIRE-BLAZE
LPJ-GUESS-SPITFIRE
ORCHIDEE-MICT-SPITFIRE
SSiB4
Analysis
Weights
Present-day Simulation
Counterfactual
Factual
Density (-)
Burned Area Relative Anomaly (-)
weight
Model

Model		CLASSIC	INFERNO	LPJ-GUESS-SIMFIRE-BLAZE	LPJ-GUESS-SPITFIRE	ORCHIDEE-MICT-SPITFIRE	SSiB4/TRIFFID	VISIT
Fire Model		CLASSIC	INFERNO	SIMFIRE	SPITFIRE	SPITFIRE	Li	After [51]
Land / Vegetation		CLASSIC	JULES	LPJ-GUESS	LPJ-GUESS	ORCHIDEE	SSiB	VISIT
Dynamic Veg	**Physiology**	Yes	Yes, via TRIFFID	Yes	Yes	Yes	Yes, via TRIFFID	Yes
	LAI	Yes	Yes, via TRIFFID	Yes	Yes	Yes	Yes	Yes
	Bio-geography	No	Yes, via TRIFFID	Yes	Yes	Yes	Yes	No
Nitrogen Cycle		Yes	Yes	Yes	Yes	No	Yes	Yes, but C-N coupling is limited
No. PFTs		9	13	17	17	19	7	33 (biome types)
No. Soil Layers		20	4	2	2	11	3	2
Fuel		Vegetation and litter	Vegetation & top soil layer as proxy for litter	Vegetation, litter	Litter	Vegetation and litter	Vegetation and litter	Litter
Ignitions	**Natural**	Prescribed lightning	Prescribed lightning	SIMFIRE describes annual BA + fire-climatology -> daily BA used as Fire-Probability	Prescribed lightning	Prescribed lightning	Prescribed lightning	Probabilistic based on fuel wetness
	Anthropogenic	Prescribed population density	Prescribed Population density	SIMFIRE includes suppression by humans	Prescribed population density	Prescribed population density	Prescribed population density	No
Suppression		Prescribed population density	Crops, population density	Crops (100%), prescribed population density (Hyde3.1)	Crops, population density	Prescribed population density, crops	Prescribed population density and GDP	Low fuel load
Spread		Wind speed and soil moisture	None	Daily BA (no explicit spread)	Rothermel equations including wind speed, tree fraction, grass fraction, fuel moisture, fuel load and characteristics	wind speed, tree fraction, grass fraction, fuel moisture, fuel load	Wind speed and soil moisture	None
Model inputs		SW & LW radiation, precipitation, air temperature, specific humidity, wind speed, atmospheric pressure, population density, lightning	SW & LW radiation, precipitation, air temperature, specific humidity, wind speed, population density, lightning	SW radiation, precipitation, air temperature (mean, min, max), relative humidity, wind speed	SW radiation, precipitation, air temperature, specific humidity, wind speed, atmospheric pressure, population density, lightning	SW & LW radiation, precipitation, air temperature, specific humidity, wind speed, atmospheric pressure, PFT map, population density	SW & LW radiation, precipitation, air temperature, specific humidity, wind speed, atmospheric pressure, population density, and GDP, peat map, land cover change	Air temperature, precipitation, air vapor pressure, cloudiness, wind
Resolution		1 deg	0.5 deg	0.5 deg	0.5 deg	0.5 deg	0.5 deg	0.5 deg
References		[52]	[53–55]	[48,56,57]	[48,56,58,59]	[60,61]	[62–65]	[66]

		CLASSIC	JULES	LPJ-GUESS-SIMFIRE-BLAZE	LPJ-GUESS-SPITFIRE	ORCHIDEE-MICT-SPITFIRE	SSiB4	VISIT
FireCCI5.1	NME_3 Ranked	*0.85*	*0.92*	*0.8*	*0.94*	*1.41*	*0.54*	*1.21*
	NME_3 Annual	*0.71*	*0.85*	*1.08*	*1.26*	*1.66*	*0.78*	*1.58*
GFED5	NME_3 Ranked	*0.87*	*0.94*	*0.91*	*1.17*	*1.49*	*0.73*	*1.26*
	NME_3 Annual	*0.73*	*0.92*	*0.94*	*1.4*	*1.83*	*0.73*	*1.52*